

## First-principles study of twin grain boundaries in epitaxial BaSi<sub>2</sub> on Si(111)

Masakazu Baba, Masanori Kohyama, and Takashi Suemasu

Citation: *Journal of Applied Physics* **120**, 085311 (2016); doi: 10.1063/1.4961603

View online: <http://dx.doi.org/10.1063/1.4961603>

View Table of Contents: <http://scitation.aip.org/content/aip/journal/jap/120/8?ver=pdfcov>

Published by the [AIP Publishing](#)

---

### Articles you may be interested in

High density of (pseudo) periodic twin-grain boundaries in molecular beam epitaxy-grown van der Waals heterostructure: MoTe<sub>2</sub>/MoS<sub>2</sub>

*Appl. Phys. Lett.* **108**, 191606 (2016); 10.1063/1.4949559

First-principles study of the structures and electronic band properties of Bi<sub>2</sub>Te<sub>3</sub> { 0 1 1̄ 5 } nanoribbons

*AIP Advances* **5**, 067133 (2015); 10.1063/1.4922604

First-principles study of structural, electronic, vibrational, dielectric and elastic properties of tetragonal Ba<sub>2</sub>YTaO<sub>6</sub>

*J. Appl. Phys.* **116**, 144104 (2014); 10.1063/1.4897452

(Sr,Ba)(Si,Ge)<sub>2</sub> for thin-film solar-cell applications: First-principles study

*J. Appl. Phys.* **115**, 203718 (2014); 10.1063/1.4880662

Electronic properties of an epitaxial silicon oxynitride layer on a 6 H - Si C ( 0001 ) surface: A first-principles investigation

*Appl. Phys. Lett.* **91**, 061930 (2007); 10.1063/1.2769949

---

# First-principles study of twin grain boundaries in epitaxial BaSi<sub>2</sub> on Si(111)

Masakazu Baba,<sup>1</sup> Masanori Kohyama,<sup>2</sup> and Takashi Suemasu<sup>1,a)</sup>

<sup>1</sup>*Institute of Applied Physics, University of Tsukuba, Tsukuba, Ibaraki 305-8573, Japan*

<sup>2</sup>*Research Institute of Electrochemical Energy, Department of Energy and Environment, National Institute of Advanced Industrial Science and Technology, Ikeda, Osaka 563-8577, Japan*

(Received 18 March 2016; accepted 12 August 2016; published online 26 August 2016)

Epitaxial films of BaSi<sub>2</sub> on Si(111) for solar cell applications possess three epitaxial variants and exhibit a minority carrier diffusion length (ca. 9.4 μm) much larger than the domain size (ca. 0.2 μm); thus, the domain boundaries (DBs) between the variants do not act as carrier recombination centers. In this work, transmission electron microscopy (TEM) was used to observe the atomic arrangements around the DBs in BaSi<sub>2</sub> epitaxial films on Si(111), and the most stable atomic configuration was determined by first-principles calculations based on density functional theory to provide possible interface models. Bright-field TEM along the *a*-axis of BaSi<sub>2</sub> revealed that each DB was a twin boundary between two different epitaxial variants, and that Ba<sup>(II)</sup> atoms form hexagons containing central Ba<sup>(I)</sup> atoms in both the bulk and DB regions. Four possible interface models containing Ba<sup>(I)</sup>-atom interface layers were constructed, each consistent with TEM observations and distinguished by the relationship between the Si tetrahedron arrays in the two domains adjacent across the interface. This study assessed the structural relaxation of initial interface models constructed from surface slabs terminated by Ba<sup>(I)</sup> atoms or from zigzag surface slabs terminated by Si tetrahedra and Ba<sup>(II)</sup> atoms. In these models, the interactions or relative positions between Si tetrahedra appear to dominate the relaxation behavior and DB energies. One of the four interface models whose relationship between first-neighboring Si tetrahedra across the interface was the same as that in the bulk was particularly stable, with a DB energy of 95 mJ/m<sup>2</sup>. There were no significant differences in the partial densities of states and band gaps between the bulk and DB regions, and it was therefore concluded that such DBs do not affect the minority carrier properties of BaSi<sub>2</sub>. *Published by AIP Publishing.*

[<http://dx.doi.org/10.1063/1.4961603>]

## I. INTRODUCTION

The solar cell industry has been growing rapidly with the increased demand for renewable energy. Among the potential solar cell materials, Si, CdTe, and chalcopyrite have dominated the market and possess a conversion efficiency,  $\eta$ , exceeding 20%.<sup>1–3</sup> To achieve higher  $\eta$  values, photogenerated minority carriers must be extracted more efficiently to external circuits. The minority carrier diffusion length,  $L$ , is one of the most important parameters directly affecting this conversion efficiency and is detrimentally decreased by carrier recombination at defects such as dislocations and grain boundaries (GBs).<sup>4–8</sup> For example, the photocurrent density increases as  $L$  increases in the case of crystalline Si; thus, higher  $\eta$  values can be expected to lead to larger  $L$  values.<sup>9</sup> Grain boundaries in poly-crystalline Si have been investigated using electron beam-induced current and Kelvin probe force microscopy techniques to determine if they act as recombination centers.<sup>10–13</sup> It has been found that Si GBs with low values for the degree of fit ( $\Sigma$ ) do not behave as strong recombination sites.<sup>13</sup> Theoretical studies show that this effect can be attributed to differences in the electronic structures resulting from various types of GBs.<sup>14</sup> As another example, twin boundaries in Cu(In,Ga)Se<sub>2</sub> do not function as strong recombination sites.<sup>15</sup> This is thought to be caused either by a change in the Cu(In,Ga)Se<sub>2</sub>

composition ratio or by band bending at the GBs.<sup>16–18</sup> Theoretical studies show that there is a valence-band offset at the GBs owing to the difference in the band gap,  $E_g$ , between the bulk and GB regions.<sup>19</sup> For this reason, the effect of the GBs upon minority carrier properties will vary between solar cell materials. It is therefore essential to understand the properties of the GBs in each material.

Orthorhombic BaSi<sub>2</sub> is a promising candidate for thin-film solar cell applications because it is expected to generate an  $\eta$  value of approximately 25% in a 2-μm-thick p-n junction diode.<sup>20</sup> Both theoretical and experimental studies have confirmed that this material exhibits an  $E_g$  of approximately 1.3 eV and has a high absorption coefficient,  $\alpha$ , exceeding  $3 \times 10^4 \text{ cm}^{-1}$  for photon energies above 1.5 eV.<sup>21–24</sup> In this compound, a direct transition occurs at approximately 0.1 eV above  $E_g$ , which may explain why experimental studies have found that BaSi<sub>2</sub> exhibits an elevated  $\alpha$  value despite its indirect band gap.<sup>21,23</sup> Another attractive feature of this material is the large  $L$  of 9.4 μm in the *a* axis-oriented undoped n-BaSi<sub>2</sub> epitaxial films on Si(111).<sup>25</sup> These films possess three epitaxial variants rotated around the surface normal at 120° with respect to one another.<sup>26</sup> The domain size in BaSi<sub>2</sub> on Si(111) can be varied from 0.2 to 4.0 μm, while the domain size for BaSi<sub>2</sub> on Si(001) can vary from 1.0 to 9.0 μm.<sup>27–29</sup> With regard to domain size, therefore, the use of Si(001) is preferable because the number of domain boundaries (DBs) between the BaSi<sub>2</sub> epitaxial variants will decrease. However,  $L$  can be as low as 1.5 μm for undoped

<sup>a)</sup>Electronic mail: suemasu@bk.tsukuba.ac.jp

n-BaSi<sub>2</sub> on Si(001),<sup>30</sup> which degrades the photoresponsivity of the film significantly compared with that of BaSi<sub>2</sub> on Si(111).<sup>31,32</sup> We have attributed the high  $L$  and pronounced photoresponsivity of undoped n-BaSi<sub>2</sub> on Si(111) to the downward band bending at the DBs, as determined by Kelvin probe force microscopy, which may restrict photo-generated minority carriers (holes) from the DBs.<sup>33,34</sup> In contrast, upward band bending is observed at the DBs in the case of BaSi<sub>2</sub> on Si(001),<sup>33</sup> meaning that the photogenerated minority carriers are directed toward defective DBs. Plan-view transmission electron microscopy (TEM) observations have shown that there are numerous defective DBs in BaSi<sub>2</sub> on Si(001), whereas many sharp straight DBs parallel to the (011) or (0-11) planes are found in BaSi<sub>2</sub> on Si(111).<sup>25</sup> However, the atomic arrangement around the DBs in BaSi<sub>2</sub> on Si(111) is yet to be investigated in detail. In this work, we attempted to clarify the stable atomic configurations of these DBs using high-resolution plan-view TEM and first-principles calculations. We initially constructed DB interface models that were consistent with TEM observations and then obtained the most stable atomic configuration via relaxation calculations based on density functional theory (DFT). Finally, we examined the electronic structures of DBs by assessing the partial densities of states (DOSs) of the Si and Ba atoms around the DBs.

## II. METHODS

### A. High-resolution plan-view TEM observations

An ion-pumped molecular beam epitaxy (MBE) system equipped with a standard Knudsen cell for Ba and an electron-beam evaporation source for Si was employed in this study. In preparation for testing, a 70-nm-thick  $a$  axis-oriented BaSi<sub>2</sub> epitaxial film was formed on Si(111) by MBE. The details of the growth procedure have been described in a previous report.<sup>26</sup> From reflection high-energy electron diffraction and  $\theta$ - $2\theta$  X-ray diffraction (XRD) patterns, we confirmed epitaxial growth of the film. It was also found that the BaSi<sub>2</sub> film was not strained but relaxed from the XRD peak positions. Plan-view TEM samples prepared by mechanical polishing and ion milling were observed along the  $a$ -axis of the BaSi<sub>2</sub> using an FEI instrument (Tecnai Osiris) operated at 200 kV.

### B. Computational details

We obtained the energies and stable configurations of DB interface models by DFT calculations using the projector-augmented wave method<sup>36</sup> within the Perdew–Wang generalized gradient approximation<sup>37</sup> employing the VASP code.<sup>35</sup> The cut-off energy of the plane-wave basis sets was 360 eV. For  $k$  points in the Brillouin zone, a  $6 \times 8 \times 4$  Monkhorst–Pack mesh<sup>38</sup> was used for a perfect crystal (with an orthorhombic cell), and a similar  $k$ -point mesh density was adopted for surface and interface supercells. The lattice constants and inner atomic positions of the perfect crystal were optimized via total energy minimization using a conjugate-gradient routine. The optimized lattice constants used were  $a = 0.8963$  nm,  $b = 0.6776$  nm, and  $c = 1.1567$  nm, which are in good agreement with previous experimental and theoretical results.<sup>22,39–41</sup>

Please note that we did not take the influence of strain induced in BaSi<sub>2</sub> by the Si(111) substrate into consideration. This is because it was found from XRD measurements on the 70 nm-thick epitaxial films of BaSi<sub>2</sub> that they were not strained but relaxed. Furthermore, in a solar cell application, we expect the BaSi<sub>2</sub> layer thickness to be more than 1  $\mu\text{m}$ ; thus, it is reasonable to think that such BaSi<sub>2</sub> films are relaxed.

Figure 1(a) shows the atomic positions of Ba and Si in an orthorhombic BaSi<sub>2</sub> unit cell, while Fig. 1(b) presents the positions along the  $a$ -axis, using the VESTA program to visualize the structures.<sup>42,43</sup> Barium disilicide belongs to the  $Pnma$  space group and its unit cell contains eight formula units. The stoichiometric description of the unit cell is Ba<sub>8</sub>Si<sub>16</sub>. There are two crystallographically inequivalent sites for Ba (Ba<sup>(I)</sup> and Ba<sup>(II)</sup>) and three inequivalent sites for Si (Si<sup>(I)</sup>, Si<sup>(II)</sup>, and Si<sup>(III)</sup>). In addition, there are four distinct Si tetrahedra (A1, A2, B1, and B2) with varying directions and

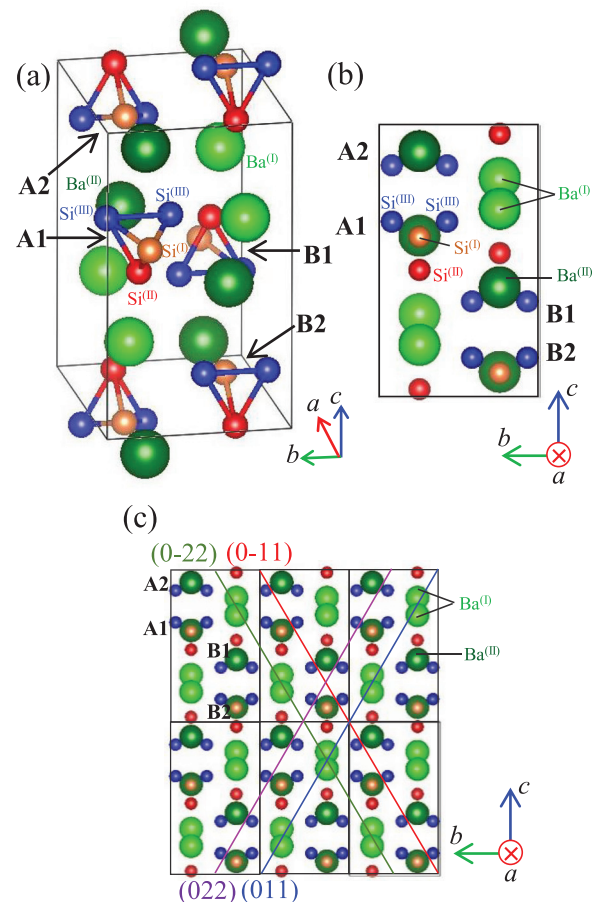


FIG. 1. (a) Crystal structure of BaSi<sub>2</sub> showing the two crystallographically inequivalent sites for Ba (Ba<sup>(I)</sup> (light green sphere) and Ba<sup>(II)</sup> (dark green sphere)) and the three for Si (Si<sup>(I)</sup> (orange sphere), Si<sup>(II)</sup> (red sphere), and Si<sup>(III)</sup> (purple sphere)) in the unit cell of BaSi<sub>2</sub>. Four Si tetrahedra (A1, A2, B1, and B2) are grouped into sets of two, depending upon the position of the Si<sup>(I)</sup> atom. Si<sup>(I)</sup> is located in the negative  $a$ -axis direction with respect to the Si<sup>(II)</sup>-Si<sup>(III)</sup>-Si<sup>(III)</sup> isosceles in the A1 and A2 tetrahedra, whereas it is in the positive  $a$ -axis direction with respect to the B1 and B2 tetrahedra. (b) Projection of the BaSi<sub>2</sub> unit cell on the  $b$ - $c$  plane. In each Si tetrahedron, one Si<sup>(I)</sup> atom and two Si<sup>(III)</sup> atoms have similar  $a$ -axis coordinates, and form an isosceles triangle. (c) Extended projection of the BaSi<sub>2</sub> cells showing the (011) (blue line), (022) (purple line), (0-11) (red line), and (0-22) (green line) crystal planes. The (011) and (0-22) planes include Ba<sup>(I)</sup> atoms, while the (0-11) and (022) planes include Ba<sup>(II)</sup> and Si tetrahedra.

positions that can be mutually translated by symmetric operations. In each Si tetrahedron, the two  $\text{Si}^{(\text{III})}$  atoms (purple spheres in Fig. 1) and the single  $\text{Si}^{(\text{II})}$  atom (red sphere in Fig. 1) have similar  $a$ -axis coordinates and form an isosceles triangle. The  $\text{Ba}^{(\text{II})}$  atom is located between two Si tetrahedra along the  $a$ -axis, whereas  $\text{Ba}^{(\text{I})}$  atoms are located between the arrays of Si tetrahedra and  $\text{Ba}^{(\text{II})}$ . In the case of A1 and A2, the  $\text{Si}^{(\text{I})}$  atoms are positioned in the negative direction with respect to the isosceles triangle  $\text{Si}^{(\text{III})}$ - $\text{Si}^{(\text{III})}$ - $\text{Si}^{(\text{III})}$ , while they are located in the positive direction for B1 and B2. In contrast, within the A1-A2 or B1-B2 pairs, the directions of each member of the pair with respect to the isosceles triangles are opposite to one another along the  $c$ -axis. Figure 1(c) shows the crystal planes that are parallel to (011) or (0-11) and that constitute the DBs in  $\text{BaSi}_2$ , as confirmed by plan-view TEM.<sup>25</sup> In these images, two different atomic layers are observed: a layer that includes  $\text{Ba}^{(\text{I})}$  atoms as (011) or (0-22) and a layer that includes both  $\text{Ba}^{(\text{II})}$  atoms and Si tetrahedra as (0-11) or (022). These are hereafter referred to as the  $\text{Ba}^{(\text{I})}$ -type and  $\text{Ba}^{(\text{II})}$ Si-type interfaces, respectively, and are included in the surface and interface models, as explained below.

Figure 2(a) presents one period of a (011) surface slab forming a  $\text{Ba}^{(\text{I})}$ -type twin boundary model, indicating the position of the surface at which the  $\text{Ba}^{(\text{I})}$  arrays are divided into two (purple arrows). This slab contains twice as many atoms as a  $\text{BaSi}_2$  unit cell per period. Point O, denoted

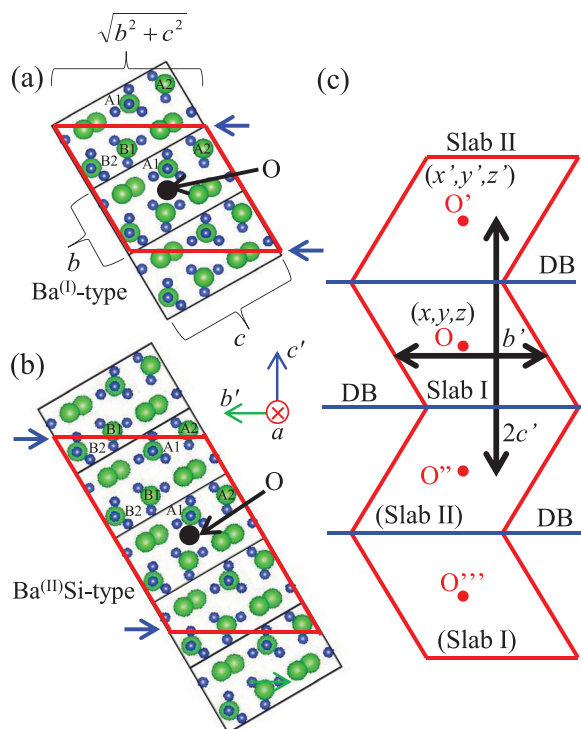


FIG. 2. (a)  $\text{Ba}^{(\text{I})}$ -type surface slab containing a (011) or (0-22) plane. (b)  $\text{Ba}^{(\text{II})}$ Si-type surface slab containing a (0-11) or (022) plane. (c) Construction of a twin-boundary supercell. A surface slab of  $\text{Ba}^{(\text{I})}$ -type or  $\text{Ba}^{(\text{II})}$ Si-type (slab I) and a symmetrically transformed slab (slab II) are stacked in an alternating fashion in the vertical direction while maintaining inversion symmetry. Purple lines show the positions of the domain boundary (DB). Points O, O', O'', and O''' are located in the center of each slab. In (a) and (b), specific Si tetrahedra are labeled A1, A2, B1, and B2.

by the black dots in Figs. 2(a) and 2(b), is the center of inversion. Figure 2(b) shows one period of a (022) surface slab forming a  $\text{Ba}^{(\text{II})}$ Si-type twin boundary model, containing three times the number of atoms in a  $\text{BaSi}_2$  unit cell. In each supercell, a  $10 \text{ \AA}$  vacuum layer was inserted between repeated slabs in the vertical direction. Following relaxation, the surface energy,  $E_{\text{surface}}$ , is given by

$$E_{\text{surface}} = \frac{E_{\text{slab1}} - E_{\text{bulk}}}{2S}, \quad (1)$$

where  $E_{\text{slab1}}$  is the total energy of the slab supercell,  $E_{\text{bulk}}$  is the total energy of a perfect crystal including the same number of atoms as one period of the surface slab, and  $S = a \times \sqrt{b^2 + c^2}$  is the surface area ( $ab'$ ) of a single period. There are two means of setting the initial surface configuration for a  $\text{Ba}^{(\text{II})}$ Si-type surface slab, as shown in Fig. 3. One approach involves cutting along the Si tetrahedral (dotted line in Fig. 3), while the other involves going around the Si tetrahedra (red line in Fig. 3). The calculated  $E_{\text{surface}}$  values were  $3870$  and  $837 \text{ mJ/m}^2$  for the former and latter approaches, respectively. We therefore chose the latter approach to construct a  $\text{Ba}^{(\text{II})}$ Si-type twin boundary model. It should also be noted that the value of  $E_{\text{surface}}$  was  $648 \text{ mJ/m}^2$  for the  $\text{Ba}^{(\text{I})}$ -type surface (Fig. 2(a)).

In this work, these two types of surface slabs were employed for twin boundaries to maintain surfaces with bulk-like stoichiometries. Cleaving the bulk crystal into two using the planes shown in Figs. 1(c) or 3 results in two equivalent surfaces, wherein each surface has the desired stoichiometry; thus, our twin configuration models preserve the bulk stoichiometry. In the present study, we felt that this was a necessary precondition for stable DBs, although it should be noted that we do not exclude other possibilities that may exist. However, using this approach, we constructed

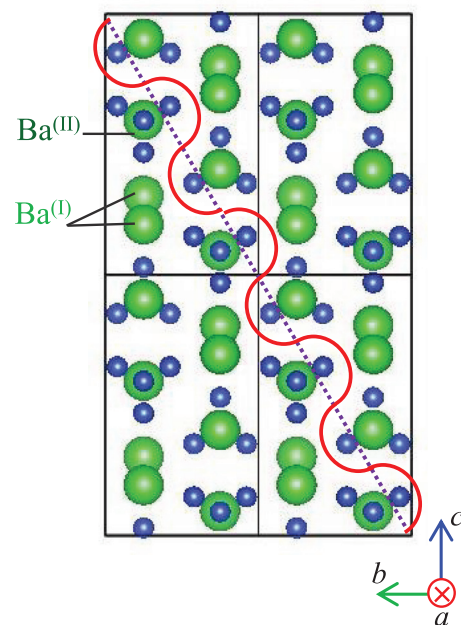


FIG. 3. Detailed structure of a  $\text{Ba}^{(\text{II})}$ Si-type domain boundary (DB). The dotted line shows the position of a (0-11) plane, while the red zigzag line that goes around the Si tetrahedra indicates the selected  $\text{Ba}^{(\text{II})}$ Si-type DB.

a highly probable interface model that is consistent with TEM observations, as described below.

Figure 2(c) summarizes the procedure used to construct a supercell of a twin boundary. A Ba<sup>(I)</sup>-type or Ba<sup>(II)</sup>Si-type surface slab (slab I) and a symmetrically transformed slab (slab II) are stacked in an alternating fashion in the vertical direction, maintaining the inversion symmetry. Slab II is formed by a mirror operation of slab I with respect to the (011) plane ( $a$ - $b'$  plane), or by a mirror operation with respect to both (011) ( $a$ - $b'$  plane) and (100) ( $b'$ - $c'$  plane) planes. The latter transformation corresponds to a  $C_2$  rotation around the  $b'$ -axis. Point O in Fig. 2(c) is the inversion center of slab I and points O' and O'' are symmetrically translated from point O. The unit cell is constructed from vectors with lengths  $a$  and  $b'$  ( $=\sqrt{b^2 + c^2}$ ) along the  $a$ - and  $b'$ -axes, respectively, as well as the vector from O'' to O' along the  $c'$ -axis. In addition, there are two degrees of freedom for rigid body translations (RBTs) between the slabs along the interface (i.e., along the  $a$ - and  $b'$ -axes) and one degree of freedom for expansion or compression normal to the interface. The unit cell maintains inversion symmetry with respect to point O and contains two equivalent DB interfaces. Thus, the RBTs are included twice in the vector from O'' to O'. As a result, the DB energy,  $E_{DB}$ , is given by

$$E_{DB} = \frac{E_{slab2} - E_{bulk}}{2S}, \quad (2)$$

where  $E_{slab2}$  is the total energy of the DB supercell.

### III. RESULTS AND DISCUSSION

#### A. Plan-view TEM

Figure 4(a) shows a bright-field plan-view TEM image of BaSi<sub>2</sub> acquired along the  $a$ -axis. The DB runs along the upper right corner in Fig. 4(a), beginning from the position indicated by the arrow, while Fig. 4(b) is a magnified image of the white square region in Fig. 4(a). Here, the bright contrasts indicate hexagons and their centers. Based on fast Fourier transform analysis, the spacing indicated by the red broken lines in Fig. 4(b) is approximately 0.33 nm. Figure 4(c) is a schematic of the BaSi<sub>2</sub> as seen along the  $a$ -axis, where Ba<sup>(II)</sup> atoms with Si tetrahedra are located at the corners of a hexagon (indicated by the dotted red line in Figs. 4(b) and 4(c)), and Ba<sup>(I)</sup> pairs are situated around the center of the hexagon. The spacing between the two atomic layers indicated by the black broken lines in Fig. 4(c) is approximately 0.34 nm, which is a value similar to the spacing found in Fig. 4(b). From these results, we can say, that the hexagonal structure seen in Fig. 4(b), together with its center, can be attributed to Ba atoms. The same hexagonal structure is observed even at the DBs, which is an essential condition satisfied by the DB interface models.

#### B. Ba<sup>(I)</sup>-type interface models

The Ba<sup>(I)</sup>-type DB interface models were initially examined wherein surface slabs terminated by Ba<sup>(I)</sup> atoms constitute the interface (Fig. 2(a)). The surface structure can be characterized by the arrangement of arrays of Si tetrahedra and Ba<sup>(II)</sup> atoms, specified as A1, A2, B1, and B2, as seen along the  $a$ -axis. A twin-interface configuration can also be

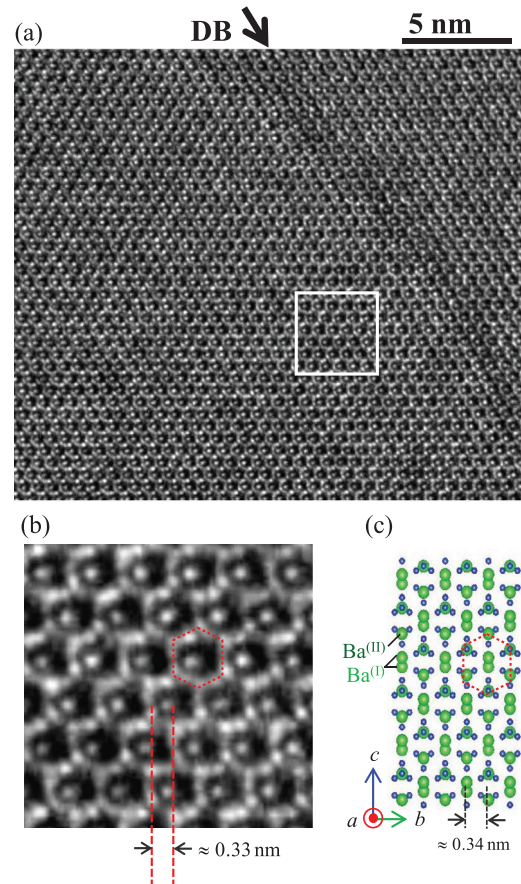


FIG. 4. (a) Plan-view TEM image acquired along the  $a$ -axis. The arrow indicates the position of the domain boundary (DB). (b) Magnified image of the region designated by the white square in (a). (c) Projection of the BaSi<sub>2</sub> cell onto the  $b$ - $c$  plane indicating an individual hexagon (red dashed line). The Ba<sup>(II)</sup> atoms are located at the corner sites of the hexagon while Ba<sup>(I)</sup> atoms are around its center.

characterized based on the arrangement of A1, A2, B1, and B2 arrays in both of the crystal slabs constituting the interface across the Ba<sup>(I)</sup>-atom interface layer. As portrayed in Fig. 5, it is possible to construct four different Ba<sup>(I)</sup>-type interface models (i.e., types I, II, III, and IV) based on this approach. Each crystal domain consists of arrays of A2-A1 and B1-B2 pairs, which are circled in Fig. 5 and wherein the broken lines indicate the interface position. The four structures in Fig. 5 have a common lower crystal domain that corresponds to the slab in Fig. 2(a). In addition, each interface structure can be distinguished by the arrays of Si tetrahedra in the upper domain that face one another across the interface, and which depend upon the symmetric operations and RBTs introduced in the upper domain. In the type I model (Fig. 5(a)), the upper domain is constructed via a mirror operation of the lower domain with respect to (011), so that the same Si tetrahedra face one another across the interface. Type II (Fig. 5(b)) is obtained by applying a half period RBT along the  $b'$ -axis ( $0.5b'$ ) to the upper domain of type I. In this structure, B1 and A2 face A2 and B1, respectively, across the interface. In type III (Fig. 5(c)), the upper domain is constructed by mirror operations with respect to both the (011) ( $a$ - $b'$  plane) and (100) ( $b'$ - $c'$  plane) planes, equivalent to a  $C_2$  rotation along the  $b'$ -axis. In this structure, B2 and A1 face A2 and B1, respectively, across the interface. This

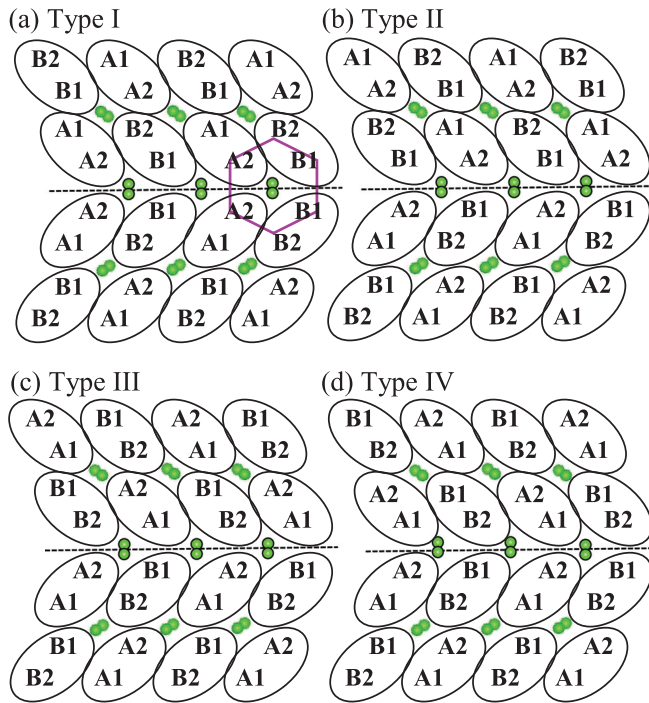


FIG. 5. Four types of  $\text{Ba}^{(\text{II})}$ -type boundary models with  $\text{Ba}^{(\text{II})}$  pairs. All of the lower domains below the domain boundary (dashed line) are common. The upper domain is formed from the lower domain by one or two mirror operations and a rigid body translation (RBT) and the A2-A1 and B1-B2 pairs are circled. (a) Type I: the upper domain is obtained by a mirror operation with respect to the (110) plane ( $a$ - $b'$  plane). (b) Type II: the upper domain is formed by introducing a RBT of  $0.5b'$  to that of type I. (c) Type III: the upper domain is obtained by introducing mirror operations with respect to both the (110) and (100) planes; that is,  $a$ - $b'$  and  $b'$ - $c'$  planes, respectively. (d) Type IV: the upper domain is formed by introducing an RBT of  $0.5b'$  to that of type III. In (a), one hexagon of the Si tetrahedral arrays of A1, A2, B1, and B2 is indicated by purple lines, and the interface is located, so that it crosses the center of the hexagon.

occurs because the Si tetrahedra A1, A2, B1, and B2 in the lower domain are, respectively, transformed to B1, B2, A1, and A2 in the upper domain. Finally, the type IV model (Fig. 5(d)) is obtained by applying a  $0.5b'$  RBT to the upper domain of type III. In this structure, A1 and B2, respectively, face A2 and B1 across the interface.

Typically, there are an infinite number of possible interface structures when considering various RBTs. However, if we restrict ourselves to the condition wherein arrays of Si tetrahedra and  $\text{Ba}^{(\text{II})}$  atoms constitute hexagons with  $\text{Ba}^{(\text{II})}$  atoms in each center, even at the interface in the projection along the  $a$ -axis, the number of possible models is greatly reduced. As shown in Fig. 5(a), a hexagon is formed by the arrays indicated by the purple lines, and the interface is located so as to cross the center of the hexagon. Figure 5 therefore presents each of the possible models when combining the four different arrays (A1, A2, B1, and B2) across the interface. These four models still permit a degree of freedom with regard to positioning an RBT along the  $a$ -axis. However, the size of this RBT along the  $a$ -axis is rather small, and a half-period RBT ( $0.5a$ ) will change type I to type IV and change type III to type II because this RBT leads to mutual transformation between A1 and A2 and between B1 and B2 in the upper domain.

Table I summarizes the  $E_{\text{DB}}$  values of the  $\text{Ba}^{(\text{I})}$ -type interface models constructed by either one or two mirror operations with various RBTs along the  $a$ - or  $b'$ -axis, wherein atoms within two atomic layers from the interface were relaxed. Structure A corresponds to the type II model in Fig. 5(b) obtained via a mirror operation with a  $0.5b'$  RBT, which is found to be somewhat unstable ( $709 \text{ mJ/m}^2$ ). Structure B is formed from type III by introducing a  $0.5a$  RBT and corresponds to the type II model in Fig. 5(b); thus, the  $E_{\text{DB}}$  value of this structure is the same as that of structure A. Structure C corresponds to the type IV model in Fig. 5(d) obtained by a mirror operation with respect to the two planes and a  $0.5b'$  RBT and appears to be relatively stable at  $233 \text{ mJ/m}^2$ . Structure D is constructed from the type I model by introducing a  $0.5a$  RBT and corresponds to the type IV model also; thus, the value of  $E_{\text{DB}}$  for this structure is the same as that for structure C.

With regard to the remaining types I and III models, it was not easy to generate stable structures from the initial configurations constructed from  $\text{Ba}^{(\text{I})}$ -type surfaces by simple relaxation because the surface  $\text{Ba}^{(\text{I})}$  atoms are positioned so close to one another across the interface. Therefore, we introduced RBTs along the  $a$ -axis, and structures E and F are formed from the type I model by introducing  $+0.25a$  or  $-0.25a$  RBTs, respectively. This leads to configurations that are intermediate between types I and IV, although the  $E_{\text{DB}}$  values remain high. Structures G and H are similarly formed from type III by introducing  $+0.25a$  or  $-0.25a$  RBTs, respectively, and exhibit energy values as high as  $4102 \text{ mJ/m}^2$ .

These results obtained from the type I and type III models may be owing to the arbitrary manner in which the initial  $\text{Ba}^{(\text{I})}$  positions are selected at the interface. This issue is discussed below when examining the  $\text{Ba}^{(\text{II})}\text{Si}$ -type interface models. Within the present examination of  $\text{Ba}^{(\text{I})}$ -type interface models, structures C and D, corresponding to the type IV model in Fig. 5(d), appear to be stable. Thus, full relaxation was performed on these two structures and  $E_{\text{DB}}$  values of  $206$ – $207 \text{ mJ/m}^2$  were obtained, as shown in Table II. These values are significantly less than the obtained  $E_{\text{surface}}$  value for these structures of  $648 \text{ mJ/m}^2$ .

### C. $\text{Ba}^{(\text{II})}\text{Si}$ -type interface models

The  $\text{Ba}^{(\text{II})}\text{Si}$ -type interface models were subsequently investigated, and Fig. 6 presents one example thereof. The

TABLE I. Domain boundary (DB) energies for the various structures present in the  $\text{Ba}^{(\text{I})}$ -type interface model obtained using one or two mirror operations in conjunction with a rigid body translation (RBT). Atoms within two atomic layers from the DB were relaxed.

Structure	RBT	DB energy ( $\text{mJ/m}^2$ )	Type
A ( $a$ - $b'$ mirror)	$0.5b'$	709	Type II
B ( $a$ - $b'$ , $b'$ - $c'$ mirror)	$0.5a$	709	Type II
C ( $a$ - $b'$ , $b'$ - $c'$ mirror)	$0.5b'$	233	Type IV
D ( $a$ - $b'$ mirror)	$0.5a$	233	Type IV
E ( $a$ - $b'$ mirror)	$0.25a$	838	NA
F ( $a$ - $b'$ mirror)	$-0.25a$	838	NA
G ( $a$ - $b'$ , $b'$ - $c'$ mirror)	$0.25a$	4102	NA
H ( $a$ - $b'$ , $b'$ - $c'$ mirror)	$-0.25a$	4102	NA

TABLE II. Domain boundary (DB) energies for the various structures of the  $\text{Ba}^{(\text{I})}$ -type interface model obtained by performing one or two mirror operations in conjunction with a rigid body translation (RBT). All atoms and lattices were relaxed.

Structure	RBT	DB energy ( $\text{mJ}/\text{m}^2$ )	Type
C ( $a$ - $b'$ mirror)	$0.5a$	207	Type IV
D ( $a$ - $b'$ , $b'$ - $c'$ mirror)	$0.5b$	206	Type IV

lower crystal slab possesses a surface with a zigzag arrangement of Si-tetrahedra and  $\text{Ba}^{(\text{II})}$  atom arrays, as shown also in Figs. 2(b) and 3. The upper slab is constructed using two mirror operations (i.e.,  $C_2$  rotation along the  $b'$ -axis) with a  $0.25b'$  RBT, resulting in the final interface indicated by the red dotted line in Fig. 6. In this case, the relationship between the two domains is similar to that in the type III structure of the  $\text{Ba}^{(\text{I})}$ -type interface models in Fig. 5. However, the initial interface region does not contain  $\text{Ba}^{(\text{I})}$  layers, but rather consists of alternating arrays of Si-tetrahedra and  $\text{Ba}^{(\text{II})}$  atoms. In Fig. 6, two bulk-like hexagons comprising A1, A2, B1, and B2 arrays are indicated by purple lines, wherein the interface is located between these two hexagons. This is in contrast to the models in Fig. 5, wherein the interface crosses the hexagon. The arrangement of the A2, A1, B1, and B2 arrays at the interface is similar to that in the bulk in this type of interface model, which reduces the freedom to select combinations of arrays in the upper crystal. In addition, there is no arbitrariness with regard to setting the initial positions of the  $\text{Ba}^{(\text{I})}$  atoms, as was encountered in the case of the  $\text{Ba}^{(\text{I})}$ -type interface models. This is because the positions of the  $\text{Ba}^{(\text{I})}$  atoms in the  $\text{Ba}^{(\text{II})}\text{Si}$ -type interface models can be considered equal to those in a perfect crystal.

Table III presents the full relaxation results for the  $\text{Ba}^{(\text{II})}\text{Si}$ -type interface models. Three structures were generated with one or two mirror operations and with different RBTs along the  $b'$ -axis. Structure B' in Table III exhibited the smallest  $E_{\text{DB}}$  value of  $95 \text{ mJ}/\text{m}^2$ , while C' has a similar structure and  $E_{\text{DB}}$  value. This value is approximately half the

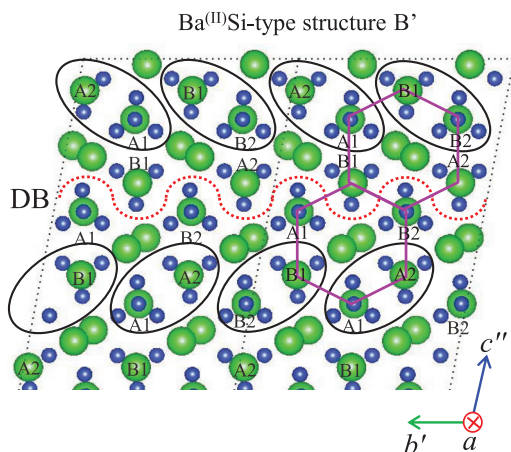


FIG. 6. Schematic of the  $\text{Ba}^{(\text{II})}\text{Si}$ -type DB supercell prior to relaxation where the A2-A1 and B1-B2 pairs are circled. Two bulk-like hexagons are indicated (purple lines), composed of Si tetrahedral arrays of A1, A2, B1, and B2. The interface is located between the two hexagons, in contrast to the models in Fig. 5.

TABLE III. Domain boundary (DB) energies for various structures of the  $\text{Ba}^{(\text{II})}\text{Si}$ -type interface model obtained by one or two mirror operations in conjunction with a rigid body translation (RBT). All atoms and lattices were relaxed.

Structure	RBT	DB energy ( $\text{mJ}/\text{m}^2$ )
A' ( $a$ - $b'$ mirror)	$0.25b'$	907
B' ( $a$ - $b'$ , $b'$ - $c''$ mirror)	$0.25b'$	95
C' ( $a$ - $b'$ , $b'$ - $c''$ mirror)	$-0.25b'$	96

smallest  $E_{\text{DB}}$  ( $206$ – $207 \text{ mJ}/\text{m}^2$ ) obtained from the  $\text{Ba}^{(\text{I})}$ -type interface models.

Figures 7(a) and 7(b) provide the respective atomic arrangements before and after the relaxation of structure C for the  $\text{Ba}^{(\text{I})}$ -type interface model in Table II, corresponding to the type IV model in Fig. 5(c). During this relaxation, the  $\text{Ba}^{(\text{I})}$  atoms at the interface became shifted along the  $b'$  axis, so that they were positioned closer to the center of the hexagon, as shown by the black broken lines in Figs. 7(a) and 7(b). Figures 7(c) and 7(d), respectively, show the atomic arrangements before and after relaxation for structure B' of the  $\text{Ba}^{(\text{II})}\text{Si}$ -type interface model in Table III. In contrast to the  $\text{Ba}^{(\text{I})}$ -type model, the shifts of the  $\text{Ba}^{(\text{II})}$  and Si atoms at the interface are relatively minimal in Figs. 7(c) and 7(d), while the  $\text{Ba}^{(\text{I})}$  pairs situated one atomic layer away from the interface (indicated by purple arrows in Fig. 7(d)) have moved such that they are aligned parallel to the  $b'$  axis. This result

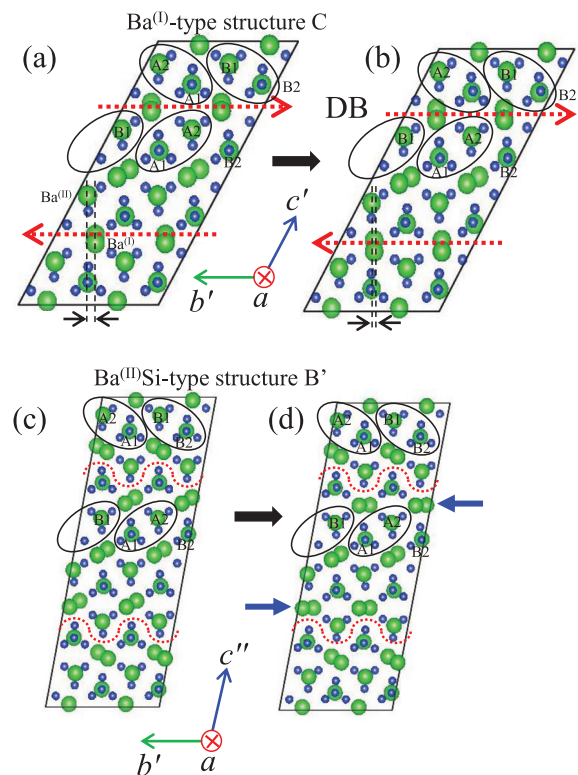


FIG. 7. Schematics of domain boundary (DB) supercells before (a) and (c) and after (b) and (d) relaxation. (a) and (b) The  $\text{Ba}^{(\text{I})}$ -type structure C DB supercell, where the positions of the  $\text{Ba}^{(\text{I})}$  atom pair around the center of each hexagon are shifted after the relaxation, as indicated by the black dashed lines. (c) and (d) The  $\text{Ba}^{(\text{II})}\text{Si}$ -type structure B' DB supercell with zigzag DBs (red dashed line). Purple arrows indicate the positions of  $\text{Ba}^{(\text{I})}$  pairs, which are parallel to the DBs. A2-A1 and B1-B2 pairs are circled.

indicates a shift of the interface position normal to the interface during the relaxation. This new interface in structure B' of the Ba<sup>(II)</sup>Si-type interface model, indicated by purple arrows in Fig. 7(d), corresponds to the type III Ba<sup>(I)</sup>-type interface model in Fig. 5(c). Even after the interface shift, the Ba<sup>(II)</sup> atoms form a hexagonal structure with a Ba<sup>(I)</sup> atom at its center in both the bulk and interface regions, which is consistent with our plan-view TEM observation shown in Fig. 4.

This interface shift in structure B' of the Ba<sup>(II)</sup>Si-type interface model can be understood by considering the behavior of the Si tetrahedra (A1, A2, B1, and B2), as shown in Figs. 8(a) and 8(b). Here, both the A1-A2 and B2-B1 pairs are circled in the bulk regions, similar to those in Fig. 8(d), and the dashed lines indicate the interface position. In the initial configuration of Fig. 8(a), the interface (red dotted line) is located between the two bulk-like hexagons. The top layer of the lower domain below the interface (labeled  $\Omega_1$ ) consists of an array of Si tetrahedra with Ba<sup>(II)</sup> atoms in the order of A1, B2, A1, and B2. This is transformed via relaxation to an A2, B1, A2, and B1 array in the bottom layer of the upper domain above  $\Omega_1$  by mirror operations with a  $0.25b'$  RBT. Following relaxation (Fig. 8(b)), the Si tetrahedra A1, B2, A1, and B2 that had belonged to the lower domain just below  $\Omega_1$  in Fig. 8(a) are now slightly shifted

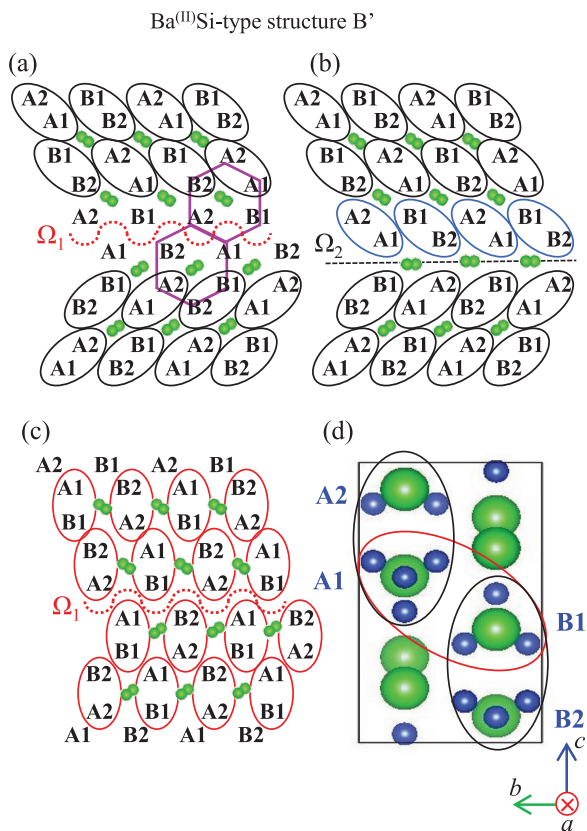


FIG. 8. (a) Schematic of Si tetrahedral pairs A1-A2 and B1-B2 (black circles) in the bulk of the Ba<sup>(II)</sup>Si-type structure B' domain boundary (DB) supercell before relaxation. Zigzag dotted red lines show the DB position, labeled as  $\Omega_1$ . (b) Formation of new pairings (purple circles) between A1-A2 and B1-B2 across the initial DB in the structure shown in (a) following relaxation. The DB is shifted from  $\Omega_1$  to  $\Omega_2$ . (c) Additional possible pairings between A1-B1 and A2-B2 (red circles), where the DB position remains the same as in (a). (d) Two types of Si tetrahedral pairs showing the structures in (a) and (b) (black circles) and those in (c) (red circle).

and rotated and belong to the upper domain (indicated by purple circles in Fig. 8(b)). Note that the directions of the Si<sup>(II)</sup>-Si<sup>(III)</sup>-Si<sup>(III)</sup> isosceles triangles in the Si tetrahedra in the lower crystal are different from those in the upper crystal, and thus the Si isosceles triangle changes direction. Figure 9 summarizes the detailed atomic structure changes induced by the relaxation and indicates all Si-Si bond lengths less than 4.005 Å. It is evident that the Si tetrahedra at the interface  $\Omega_1$  in Fig. 9(a) form the new bulk-like pairs indicated by purple circles in Fig. 9(b). Figure 9(c) also clearly shows the change in the direction of the Si<sup>(II)</sup>-Si<sup>(III)</sup>-Si<sup>(III)</sup> isosceles triangle at A1 and B2 as a result of the relaxation, where the mutual interchange between Si<sup>(II)</sup> and Si<sup>(III)</sup> indicates a change from the state associated with the lower crystal to that associated with the upper crystal. Owing to these changes, the Ba<sup>(I)</sup> pairs one layer away from interface  $\Omega_1$  transition such that they become parallel to the interface, and thereby the interface position shifts from  $\Omega_1$  to  $\Omega_2$ . The interface  $\Omega_2$  consists of a Ba<sup>(I)</sup> layer similar to that in the Ba<sup>(I)</sup>-type interface models. From the arrangement of the Si tetrahedra near  $\Omega_2$ , it is clear that the new interface corresponds to the type III model in Fig. 5(c).

Here, we can make additional proposals regarding the re-arrangement of Si tetrahedron pairs. In the case of the initial configuration shown in Fig. 8(c), we can consider another approach that pairs the Si tetrahedra in the vertical direction, as indicated by the red circles. Note that the pairs

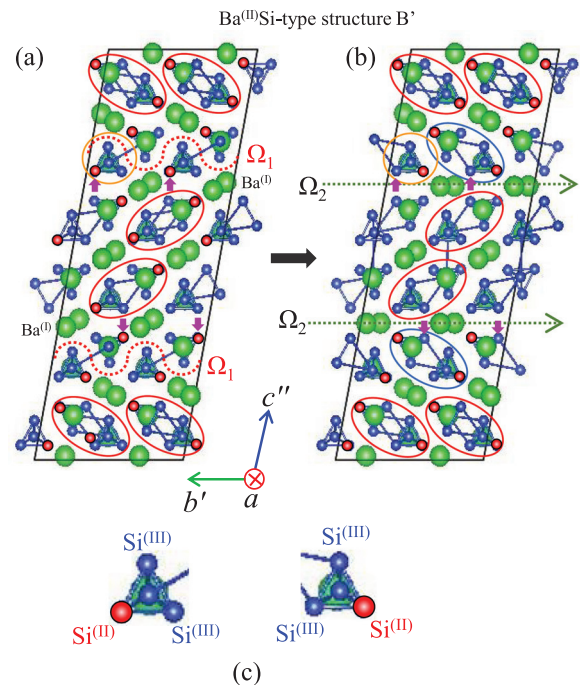


FIG. 9. Schematics of the Ba<sup>(II)</sup>Si-type structure B' domain boundary (DB) supercell (a) before and (b) after relaxation, where Si-Si bond lengths less than 4.005 Å are shown. After relaxation, new pairs (purple circles) are generated across the initial DBs labeled  $\Omega_1$ . Here,  $\Omega_1$  is the initial position of the DB shown by the zigzag red dotted line in (a), while  $\Omega_2$  is considered to be a new DB shifted after relaxation. The isosceles triangles from Si<sup>(II)</sup>-Si<sup>(III)</sup>-Si<sup>(III)</sup> close to  $\Omega_1$  rotate after relaxation (see the Si<sup>(II)</sup> atoms indicated by purple arrows). (c) Enlarged images of the Si tetrahedra (orange circles) in (a) and (b). The Si atoms' positions are changed between Si<sup>(II)</sup> and Si<sup>(III)</sup> following relaxation.

below and above the interface  $\Omega_1$  are similar to those in the bulk, as indicated by the red circle in Fig. 8(d). Thus, if the interactions between the Si tetrahedra within this type of pairing are strong, the initial configuration in Fig. 8(c) may be stable and may eliminate the interface position shift. The present interface position shift, however, indicates that the interactions between the Si tetrahedra are stronger in the pairs indicated by black circles (Figs. 8(a) and 8(b)) than those indicated by the red circles in Fig. 8(d). The present vertical shift of the interface somewhat resembles the vertical interface shifts observed in twin or tilted boundaries in face-centered cubic (fcc) metals induced by parallel RBTs between two bulk crystals.<sup>44,45</sup>

Consequently, as shown in Tables II and III, the  $E_{DB}$  value of the  $\text{Ba}^{(I)}$ -type structure C interface model (type IV) is  $206 \text{ mJ/m}^2$ , while that of the  $\text{Ba}^{(II)}$ Si-type structure B' interface model (type III of the  $\text{Ba}^{(I)}$ -type interface model) is  $95 \text{ mJ/m}^2$ . We therefore assume that the twin DB structures in the  $\text{BaSi}_2$  epitaxial films on Si(111) exhibit the latter structure. We note that the most stable structure could not be obtained using the  $\text{Ba}^{(I)}$ -type interface model because the  $\text{Ba}^{(I)}$  atoms on the (110) surface in the initial structure were located too close to one another. However, in the case of the  $\text{Ba}^{(II)}$ Si-type interface model, we could set the initial positions of  $\text{Ba}^{(I)}$  and  $\text{Ba}^{(II)}$  atoms to be the same as those in the bulk crystal, and thus obtain the most stable structure via an interface shift without such difficulties.

#### D. Analysis of the two interfaces

The particular stability of the type III structure ( $95 \text{ mJ/m}^2$ ) among the  $\text{Ba}^{(I)}$ -type interface models in Fig. 5 can be explained by considering the arrangement of Si tetrahedra, as they face one another across the interface. Only in type III are the first-neighboring Si tetrahedra among the interface Si tetrahedra the same as those in the bulk material. In the lower crystal, each A2 Si tetrahedron has three neighboring Si tetrahedra (A1, B2, and B2) in the bulk, while each B1 Si tetrahedron also has three neighboring Si tetrahedra (B2, A1, and A1). At the type III model interface, the interface A2 Si tetrahedron in the lower crystal has neighboring Si tetrahedra A1 and B2 in the lower direction, and faces Si tetrahedron B2 in the upper crystal across the interface. Similarly, the B1

interface Si tetrahedron in the lower crystal has neighboring Si tetrahedra B2 and A1 in the lower direction, and faces the Si tetrahedron A1 in the upper crystal across the interface. All these first-neighboring Si tetrahedra among the interface Si tetrahedra are apparently the same as those in the bulk. The other types of interfaces in Fig. 5 do not satisfy this condition. It is well known that bulk-like first-neighbor interatomic relations are maintained in stable twin-boundary structures in diamond-structure semiconductors or in fcc metals.<sup>46</sup> It is therefore quite interesting that the bulk-like Si inter-tetrahedron relationships are maintained in the most stable twin interface within  $\text{BaSi}_2$ .

The present results concerning the relaxation behavior and relative stability of crystal configurations indicate the importance of interactions or relative positions between Si tetrahedra, and can be explained based on the bonding nature of  $\text{BaSi}_2$ . In a Si tetrahedron, each Si atom forms four  $sp^3$  hybridized orbitals and connects with three other Si atoms, which leaves one external  $sp^3$  orbital as a dangling bond. The four dangling bonds associated with each Si tetrahedron are thought to be filled with four electrons donated by two Ba atoms. In this way, each Si atom is associated with eight electrons. It is therefore safe to say, that there are strong covalent bonds between Si atoms via  $sp^3$  hybridized orbitals in addition to ionic bonding between Ba and Si in the tetrahedron, although the Ba–Si bonds will have some covalent character. The Ba atoms situated between the Si tetrahedra can therefore be considered as serving to connect the Si tetrahedra. Considering the bonding characteristics of  $\text{BaSi}_2$  in this way, the present calculation results can be understood.

With regard to the electronic properties of the DBs, Figs. 10(a) and 10(b) show partial DOSs for Ba and Si atoms, respectively, in the DB and bulk regions for the most energetically stable supercell with structure B' in Table III ( $\text{Ba}^{(II)}$ Si-type) DBs. The valence band maximum is located at  $0 \text{ eV}$ . The color lines show every contribution of a Si or Ba atom in a supercell to DOS. In the case of DB, partial DOSs of Si or Ba atoms positioned within two atomic layers from the DB are displayed, and the contributions of the other Si or Ba atoms are presented as Bulk. There are no significant differences in the  $E_g$  values and partial DOSs for the Ba

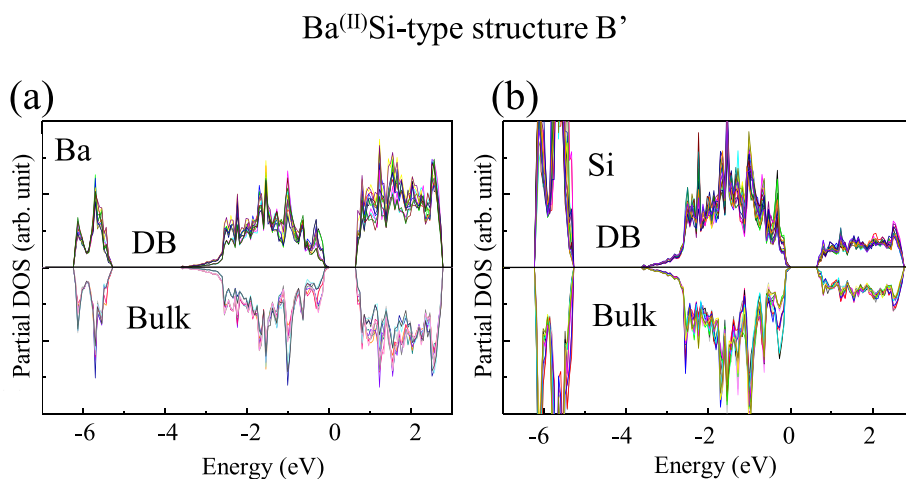


FIG. 10. Partial density of states for (a) Ba and (b) Si atoms in the domain boundary (DB) and bulk regions for supercells with structure B' in Table III ( $\text{Ba}^{(II)}$ Si-type) DBs. The valence band maximum is located at  $0 \text{ eV}$ .

and Si atoms between the bulk and interface regions. Furthermore, we do not see any localized states within the band gap for the interface regions. On the basis of these data, we can say, that the twin grain boundaries in epitaxial BaSi<sub>2</sub> on Si(111) do not degrade the electronic states. We can therefore conclude that the presence of numerous DBs in BaSi<sub>2</sub> epitaxial films on Si(111) will have no significant effect upon the minority carrier properties, and therefore will not impact the solar cell performance. Because of the gettering ability of the boundaries in polycrystalline Si, the recombination activity at these sites is greatly enhanced, especially in the case of high- $\Sigma$  boundaries.<sup>13</sup> Our previous studies have demonstrated that the diffusion coefficients of impurities such as Sb, As, and B are much higher at DBs than in grain interiors.<sup>47,48</sup> We now also know the positions of Si and Ba atoms in the most stable interface structure; thus, the present results should be applicable to various future studies, such as those concerned with the effects of impurities around DBs upon the electronic properties.

#### IV. CONCLUSION

We observed the atomic arrangements around the DBs in BaSi<sub>2</sub> epitaxial films on Si(111). The results showed that Ba atoms are situated in hexagonal structures that center around the DBs, just as in the bulk crystal. Two different twin-boundary supercells were constructed, consisting of (011) or (0-11) planes, employing first-principles calculations based on DFT. We investigated several twin-boundary interface models formed by relative translational and mirror operations to obtain the most stable structures. The most stable interface was determined and possessed an  $E_{DB}$  value of 95 mJ/m<sup>2</sup>, while another interface was identified for which  $E_{DB}$  was 206 mJ/m<sup>2</sup>. These results were both consistent with TEM observations because they involved Ba atoms positioned both within and at the center of the hexagonal structures. The various interface structures were formed using different translational operations along the interface, wherein arrays of Si tetrahedra faced one another across an interface layer consisting of Ba<sup>(I)</sup> atoms. In the most stable interface structure, the arrangement of neighboring Si tetrahedra around the DBs was the same as that in the bulk crystal. This means that the relative positions of Si tetrahedron determined the stability of the interface. There were no significant differences in the partial DOSs and  $E_g$  values around the DBs compared with values for the bulk material. We therefore conclude that DBs in BaSi<sub>2</sub> on Si(111) do not affect the minority carrier properties. This DB character indicates that BaSi<sub>2</sub> should be a suitable material for the fabrication of absorption layers in thin-film solar cell applications.

#### ACKNOWLEDGMENTS

The TEM observations were performed with the assistance of Mr. N. Saitoh and Dr. N. Yoshizawa of the Electron Microscope Facility, AIST, Japan. This work was financially supported by the Japan Science and Technology Agency and by a Grant-in-Aid for Scientific Research A (15H02237) from the Japan Society for the Promotion of Science.

- <sup>1</sup>M. A. Green, *Prog. Photovoltaics: Res. Appl.* **17**, 183 (2009).
- <sup>2</sup>O. Schultz, S. W. Glunz, and G. P. Willeke, *Prog. Photovoltaics: Res. Appl.* **12**, 553 (2004).
- <sup>3</sup>P. Jackson, D. Hariskos, E. Lotter, S. Paetel, R. Wuerz, R. Menner, W. Wischmann, and M. Powalla, *Prog. Photovoltaics: Res. Appl.* **19**, 894 (2011).
- <sup>4</sup>T. Daud, K. M. Koliwad, and F. G. Allen, *Appl. Phys. Lett.* **33**, 1009 (1978).
- <sup>5</sup>T. Kieliba, S. Riepe, and W. Warta, *J. Appl. Phys.* **100**, 063706 (2006).
- <sup>6</sup>L. L. Kazmerski, *Solid State Electron.* **21**, 1545 (1978).
- <sup>7</sup>L. L. Kazmerski, P. Sheldon, and P. J. Ireland, *Thin Solid Films* **58**, 95 (1979).
- <sup>8</sup>J. D. Zook, *Appl. Phys. Lett.* **37**, 223 (1980).
- <sup>9</sup>B. M. Kayes, H. A. Atwater, and N. S. Lewis, *J. Appl. Phys.* **97**, 114302 (2005).
- <sup>10</sup>Z.-J. Wang, S. Tsurekawa, K. Ikeda, T. Sekiguchi, and T. Watanabe, *Interface Sci.* **7**, 197 (1999).
- <sup>11</sup>S. Tsurekawa, K. Kido, and T. Watanabe, *Mater. Sci. Eng. A* **462**, 61 (2007).
- <sup>12</sup>S. Tsurekawa, H. Takahashi, Y. Nishibe, and T. Watanabe, *Philos. Mag.* **93**(10–12), 1413 (2013).
- <sup>13</sup>J. Chen, T. Sekiguchi, D. Yang, F. Yin, K. Kido, and S. Tsurekawa, *J. Appl. Phys.* **96**, 5490 (2004).
- <sup>14</sup>M. Kohyama and R. Yamamoto, *Phys. Rev. B* **50**, 8502 (1994).
- <sup>15</sup>M. Kawamura, T. Yamada, N. Suyama, A. Yamada, and M. Konagai, *Jpn. J. Appl. Phys.* **49**, 062301 (2010).
- <sup>16</sup>M. J. Hetzer, Y. M. Strzhemechny, M. Gao, M. A. Contreras, A. Zunger, and L. J. Brillson, *Appl. Phys. Lett.* **86**, 162105 (2005).
- <sup>17</sup>D. Abou-Ras, B. Schaffer, M. Schaffer, S. S. Schmidt, R. Caballero, and T. Unold, *Phys. Rev. Lett.* **108**, 075502 (2012).
- <sup>18</sup>U. Rau, K. Taretto, and S. Siebentritt, *Appl. Phys. A* **96**, 221 (2009).
- <sup>19</sup>C. Persson and A. Zunger, *Appl. Phys. Lett.* **87**, 211904 (2005).
- <sup>20</sup>T. Suemasu, *Jpn. J. Appl. Phys.* **54**, 07JA01 (2015).
- <sup>21</sup>K. Morita, Y. Inomata, and T. Suemasu, *Thin Solid Films* **508**, 363 (2006).
- <sup>22</sup>D. B. Migas, V. L. Shaposhnikov, and V. E. Borisenko, *Phys. Status Solidi B* **244**, 2611 (2007).
- <sup>23</sup>K. Toh, T. Saito, and T. Suemasu, *Jpn. J. Appl. Phys.* **50**, 068001 (2011).
- <sup>24</sup>M. Kumar, N. Umezawa, and M. Imai, *Appl. Phys. Express* **7**, 071203 (2014).
- <sup>25</sup>M. Baba, K. Toh, K. Toko, N. Saito, N. Yoshizawa, K. Jiptner, T. Sekiguchi, K. O. Hara, N. Usami, and T. Suemasu, *J. Cryst. Growth* **348**, 75 (2012).
- <sup>26</sup>Y. Inomata, T. Nakamura, T. Suemasu, and F. Hasegawa, *Jpn. J. Appl. Phys.* **43**(4A), L478 (2004).
- <sup>27</sup>K. Toh, K. O. Hara, N. Usami, N. Saito, N. Yoshizawa, K. Toko, and T. Suemasu, *J. Cryst. Growth* **345**, 16 (2012).
- <sup>28</sup>K. Toh, K. O. Hara, N. Usami, N. Saito, N. Yoshizawa, K. Toko, and T. Suemasu, *Jpn. J. Appl. Phys.* **51**, 095501 (2012).
- <sup>29</sup>M. Baba, K. Nakamura, W. Du, M. Ajmal Khan, S. Koike, K. Toko, N. Usami, N. Saito, N. Yoshizawa, and T. Suemasu, *Jpn. J. Appl. Phys.* **51**, 098003 (2012).
- <sup>30</sup>M. Baba, K. Watanabe, K. O. Hara, K. Toko, T. Sekiguchi, N. Usami, and T. Suemasu, *Jpn. J. Appl. Phys.* **53**, 078004 (2014).
- <sup>31</sup>S. Koike, M. Baba, R. Takabe, N. Zhang, W. Du, K. Toko, and T. Suemasu, *Jpn. J. Appl. Phys.* **53**, 058007 (2014).
- <sup>32</sup>W. Du, M. Suzuno, M. Ajmal Khan, K. Toh, M. Baba, K. Nakamura, K. Toko, N. Usami, and T. Suemasu, *Appl. Phys. Lett.* **100**, 152114 (2012).
- <sup>33</sup>M. Baba, S. Tsurekawa, K. Watanabe, W. Du, K. Toko, K. O. Hara, N. Usami, T. Sekiguchi, and T. Suemasu, *Appl. Phys. Lett.* **103**, 142113 (2013).
- <sup>34</sup>D. Tsukahara, M. Baba, S. Honda, Y. Imai, K. O. Hara, N. Usami, K. Toko, J. H. Werner, and T. Suemasu, *J. Appl. Phys.* **116**, 123709 (2014).
- <sup>35</sup>G. Kresse and D. Joubert, *Phys. Rev. B* **59**, 1758 (1999).
- <sup>36</sup>P. E. Blöchl, *Phys. Rev. B* **50**, 17953 (1994).
- <sup>37</sup>J. P. Perdew and Y. Wang, *Phys. Rev. B* **45**, 13244 (1992).
- <sup>38</sup>H. J. Monkhorst and J. D. Pack, *Phys. Rev. B* **13**, 5188 (1976).
- <sup>39</sup>J. Evers, *J. Solid State Chem.* **32**, 77 (1980).
- <sup>40</sup>H. Schäfer, K. H. Janzou, and A. Weiss, *Angew. Chem., Int. Ed.* **2**, 393 (1963).
- <sup>41</sup>M. Imai and T. Hirano, *J. Alloy Compd.* **224**, 111 (1995).
- <sup>42</sup>K. Momma and F. Izumi, *J. Appl. Crystallogr.* **41**, 653 (2008).
- <sup>43</sup>K. Momma and F. Izumi, *J. Appl. Crystallogr.* **44**, 1272 (2011).

- <sup>44</sup>H. Van Swygenhoven and P. M. Derlet, *Phys. Rev. B* **64**, 224105 (2001).
- <sup>45</sup>C. Molteni, N. Marzari, M. C. Payne, and V. Heine, *Phys. Rev. Lett.* **79**, 869 (1997).
- <sup>46</sup>J. R. Morris, C. L. Fu, and K. M. Ho, *Phys. Rev. B* **54**, 132 (1996).

- <sup>47</sup>K. Nakamura, M. Baba, K. M. Ajmal, W. Du, M. Sasase, K. O. Hara, N. Usami, K. Toko, and T. Suemasu, *J. Appl. Phys.* **113**, 053511 (2013).
- <sup>48</sup>N. Zhang, K. Nakamura, M. Baba, K. Toko, and T. Suemasu, *Jpn. J. Appl. Phys.* **53**, 04ER02 (2014).